

Internal excitation and superfocusing of surface plasmon polaritons on a silver-coated optical fiber tip

W. Ding,* S. R. Andrews, and S. A. Maier

*Centre for Photonics and Photonic Materials, Department of Physics, University of Bath, Claverton Down,
Bath BA2 7AY, United Kingdom*

(Received 17 March 2007; published 25 June 2007)

We have theoretically studied the conversion of radially polarized waveguide modes of a tapered optical fiber into surface plasmon polaritons (SPPs) propagating at the outer surface of an apertureless silver-coated optical tip. Optimization of this process is important in exploiting SPP superfocusing in scanning near-field optical microscopy without the need for external illumination. Our approach is based on analyzing the evolution of the local modal index as a function of the fiber radius. The influence of mode projection, intermodal coupling, and metal dissipation are treated analytically, while a numerical finite integration technique is used to model radiation coupling. The results identify and quantify the mode conversion processes that need to be taken into account. We estimate that at least 10% of the modal energy in an uncoated fiber taper can be fed into the superfocusing mode at a silver-coated tip.

DOI: [10.1103/PhysRevA.75.063822](https://doi.org/10.1103/PhysRevA.75.063822)

PACS number(s): 42.25.Bs, 41.20.Jb, 03.50.De, 42.79.-e

I. INTRODUCTION

The last two decades have witnessed continuously increasing activity in scanning near-field optical microscopy (SNOM) [1–10], whose central goal is imaging and spectroscopy on the nanometer scale. In order to break the diffraction limit on spatial resolution, metal-coated, tapered optical fiber probes have been developed either with [2–5] or without [6–9] apertures at the apex. In the widely used apertured scheme, the optical energy is delivered to or collected from the sample through a 30–50 nm opening at the probe apex. The resolution is determined by the practically usable aperture size, which is limited by the cutoff of the waveguide modes in the metal-coated fiber tip [5,8] and by field penetration into the metal. For apertures below cutoff, the optical throughput is drastically reduced. The alternative method utilizes apertureless metal-coated tips, which show strong field confinement and enhancement upon external illumination due to the lightning-rod effect and the excitation of localized tip plasmons. Plasmons at the tip apex can be excited by direct illumination [7–9] or by using a prism-based total-internal-reflection configuration [6]. Although resolution as good as 3 nm has been demonstrated using this method [10], less than 1 part in 10^5 of the excitation power is typically transferred to the sampled volume. Hence tip-height modulation or nonlinear optical techniques must generally be used to remove the strong far-field background, the system complexity is increased, and there can be severe sample heating.

A variation on the above approaches has recently been discussed [11–14]. It exploits the fact that a metal wire can support surface plasmon polaritons (SPPs) strongly confined near the metal boundary [15]. If the wire is tapered to a point then the SPP becomes more plasmonlike as it propagates towards the apex. There is a dramatic reduction in phase and group velocity, shortening of the propagation wavelength, and enhancement of the local field amplitude when the radius

becomes small compared with the free space wavelength, a phenomenon known as superfocusing [11–14,16,17]. The field confinement, and thus spatial resolution, is mainly limited by the sharpness of the tip; i.e., the radius at the apex. By applying a thin metal coating to a tapered optical fiber, one can envisage directly exciting SPPs on the outer surface by the transfer of energy from fiber modes [14], akin to SPP coupling in layered metal-dielectric geometries such as planar multilayer waveguides [18] or spherical resonator systems [19]. If the energy transfer can be made very efficient then nonlinear processes such as Raman scattering and two-photon fluorescence might, in principle, be probed with higher dynamic range. There are also other benefits such as lower system complexity and reduced sample heating.

The coupling from fiber waveguide modes to SPPs on the outer surface of a silver-coated fiber tip has recently been treated analytically by Janunts *et al.* [14]. These authors ignored metal dissipation, which is generally substantial in the visible and near-infrared, and assumed that the SPP modes confined on the inner and outer silver surfaces were nearly isolated. The coupling between the outer and inner SPP were then treated using perturbation theory but we find that this is an oversimplified and inaccurate approach. In other papers, Bouhelier *et al.* [11] and Vaccaro *et al.* [13] studied the superfocusing process using numerical methods, but their investigations were limited to the tip region and they did not consider the mode conversion processes.

In this paper, we adopt both analytical and numerical methods [based on the finite integration technique (FIT)] to study mode conversion along an apertureless, part-silver-coated fiber tip. Nonlinear optical processes are not considered. In Sec. II, we describe the evolution of the local modal indices with decreasing fiber radius, and discuss the mechanism by which SPPs are excited from fiber waveguide modes. In Sec. III, we quantitatively analyze mode propagation, which is influenced by mode projection, intermodal coupling, and metal dissipation. In Sec. IV, the coupling to radiation is numerically studied using the FIT approach. In Sec. V, we summarize the relationships between the effects

*Electronic address: pypwd@bath.ac.uk

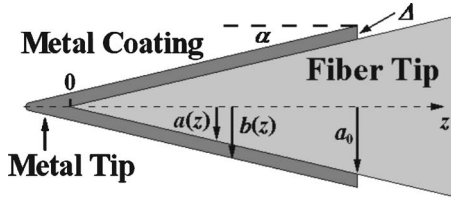


FIG. 1. Schematic of the apertureless metal-coated fiber tip.

governing propagation and the structural parameters of the fiber, and discuss how to optimize the transfer of optical power from the guided modes of a bare tapered fiber to the SPP superfocusing mode at the surface of a silver-coated tip. Conclusions are presented in Sec. VI.

II. CONVERSION FROM FIBER WAVEGUIDE TO SPP MODES

A sketch of the apertureless part-metal-coated silica fiber tip studied in this paper is shown in Fig. 1. Only the region close to the apex is coated with a metal. The inner and outer radii of the coating as a function of the axial distance z from the silica apex are $a(z)$ and $b(z)=a(z)+\Delta$, respectively. For $z < 0$ the structure simply consists of a solid metal cone with a 10 nm radius hemispherical end which helps to avoid computational singularities. The taper angle $\alpha \approx |da/dz|$, and the metal thickness Δ are taken as constant in the coated silica region, which extends from $a=0$ to $a=a_0$. The dielectric constants of silica and air are taken as 2.25 and 1, respectively. The dielectric functions of the metals used as coatings are taken from Drude-Lorentz models fitted to experimental data in Ref. [20]. Nonlocal effects in the metal have a negligible effect on the superfocusing process in the immediate vicinity of the apex [21] and are ignored in our treatment.

In local mode theory [22], the field in a weakly nonuniform optical waveguide can be expressed as a superposition of the local modes in any cross section. These local modes are the eigenmodes of the uniform waveguide obtained by infinitely stretching the local cross section along the fiber axis. In our case, the relevant modes are radially polarized. The field symmetry of such modes leads to constructive interference and field enhancement at the metal apex. This effect lies at the core of the SPP superfocusing phenomenon [11–14, 16, 17]. In free space, radial modes can be efficiently generated from linearly polarized light using, for example, sectioned phase plates [23, 24].

To solve for local modes, we first reduce Maxwell's vector equations to a scalar form using the Hertz vector $\boldsymbol{\theta} = \pi_z(r)\hat{\mathbf{a}}_z$, where $\hat{\mathbf{a}}_z$ is the unit vector along the z direction [25]. For a radially polarized mode and a cylindrical waveguide, there is no azimuthal angle dependence, and the eigenmodes satisfy the Helmholtz equation as follows:

$$\left[\partial^2 / \partial r^2 + \frac{1}{r} \partial / \partial r \right] \pi_z - [\beta^2 - n^2(r)k_0^2] \pi_z = 0, \quad (1)$$

where k_0 is the vacuum wave vector, β is the propagation constant, and $n(r)$ is the radially dependent refractive index.

The field components are then given by

$$E_z = -k_c^2 \pi_z, \quad (2a)$$

$$E_r = i\beta \partial \pi_z / \partial r, \quad (2b)$$

$$H_\phi = i\omega\epsilon \partial \pi_z / \partial r, \quad (2c)$$

where $k_c^2 = \beta^2 - n^2(r)k_0^2$, ϵ is the permittivity, and the subscript $c=in, m$, or out represents the three dielectric regions of silica core, metal coating, and surrounding medium, respectively.

The solution of Eq. (1) is

$$\pi(r) = [A_c I_0(k_c r) + B_c K_0(k_c r)] e^{i(\beta z - \omega t)}, \quad (3)$$

where I_0 and K_0 are the zero-order modified Bessel functions of first and second kind, respectively, and A_c and B_c are undetermined coefficients.

Taking into account the asymptotic properties of the modified Bessel functions as r approaches the axis and infinity, only four coefficients, A_{in} , A_m , B_m , and B_{out} , are found to be nonzero. They are related by a set of eigenequations based on the continuity requirements for E_z and H_ϕ at $r=a$ and $r=a+\Delta$ [26]. These equations can be used to obtain the mode field and propagation constant.

In order to investigate the influence of the fiber's structural parameters on the mode evolution, we calculated the modal indices (n_{eff}) as a function of the fiber radius a . Figure 2 shows the results for a metal-coated fiber surrounded by either air or an index oil with $\epsilon=2$ (curves with symbols). Silver is the preferred metal because of its relatively low loss at the wavelengths of interest but in some plots [Figs. 2(c) and 2(d)] nickel is used to study the effect of increased metal dissipation. Figure 2 also shows the modal indices for the two limiting cases where either the silica core or the surrounding medium is replaced by metal (solid curves). In the first case, the structure consists of a metal cylinder with radius b and sustains one "outer-SPP" mode. In the second case, a silica cylinder with radius a is buried in metal and sustains several fiber waveguide modes: one "inner-SPP" mode and several TM_{0n} modes. The "inner-SPP" mode is confined on the inner metal surface, and the TM_{0n} modes correspond to the counterpart TM_{0n} modes in a silica cylinder surrounded by air or oil. The hatched areas in Fig. 2 represent the radiation mode continua, which lie below the refractive indices of the external media. Any mode entering this hatched area couples to radiation and backward propagating modes and is cut off [5, 8].

In the calculations shown in Figs. 2(a)–2(d), the metal thickness is $\Delta=80$ nm, the wavelength is $\lambda_0=1.55$ μm , and the dielectric constant of the external medium is $\epsilon=1$ (air) or 2 (oil). The metal dielectric constants have values at $\lambda_0=1.55$ μm of $\epsilon_{Ag}=-103+8i$ and $\epsilon_{Ni}=-34+46i$, respectively [20]. In Figs. 2(e) and 2(f), we reduce the silver thickness to $\Delta=40$ nm [Fig. 2(e)] and change the wavelength to $\lambda_0=1.3$ μm ($\epsilon_{Ag}=-72+5i$), respectively.

A striking feature in most panels of Fig. 2 is the mode anticrossing, which happens at the intersection of the dispersion curves of the outer SPP in the metal cylinder and the inner SPP in the silica cylinder buried in the metal. The anticrossing arises from the phase-matched interaction be-

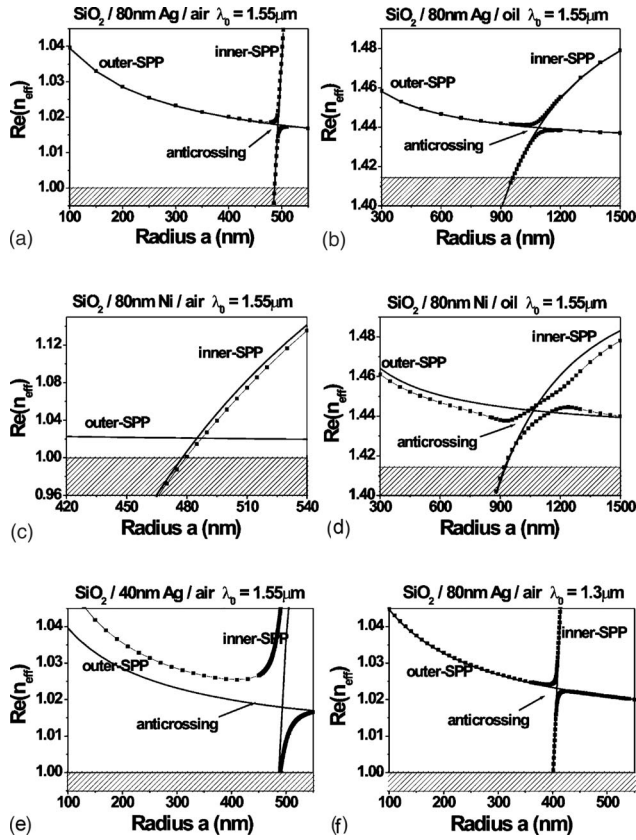


FIG. 2. [(a)–(f)]. Real part of the modal indices in a metal-coated fiber as a function of the fiber radius a (symbols). The detailed structural parameters are described in each panel.

tween modes and allows conversion of the inner SPP to the outer SPP as the fiber radius decreases. This occurs in all but Fig. 2(c), where the inner SPP is cut off. After the outer SPP is excited, the modal index increases as the apex is approached. The decrease in the wavelength of the outer SPP allows superfocusing to occur at the apex. In Fig. 2, a larger anticrossing “gap” corresponds to a stronger interaction.

Figure 2 shows that the mode anticrossing is affected by the choice of metal, external medium, metal thickness, and wavelength. For example, if nickel rather than silver is used as the fiber coating [Fig. 2(c)], the stronger metal absorption weakens the interaction between the outer and inner SPPs. These two modes are confined on their respective metal surfaces, and the anticrossing is suppressed as shown in Fig. 2(c). The inner SPP is simply cut off and there is no significant excitation of the outer SPP. Increasing the index of the external medium causes greater penetration of the outer SPP into the metal and enhances the field overlap and interaction between the outer SPP and inner SPP. The suppressed anticrossing in Fig. 2(c) then revives as shown in Fig. 2(d). For similar reasons, the metal thickness and wavelength also influence the anticrossing as shown in Figs. 2(e) and 2(f). The former determines the spatial overlap of the outer and inner SPPs and the latter alters the dielectric constant of the metal. Note that, due to the mode interaction, the modes in a metal-coated fiber are actually hybridized, but for convenience, we adopt the nomenclature “inner SPP” and “outer SPP” to re-

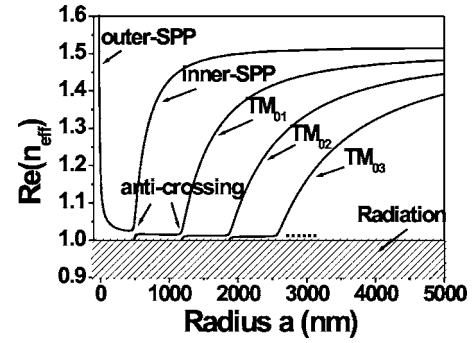


FIG. 3. Real part of the modal indices in a silver-coated fiber as a function of fiber radius a . The silver thickness is 40 nm, the external medium is air, and the wavelength is $1.55 \mu\text{m}$.

flect the character of the field distributions away from the anticrossing point. In the following sections, we limit our studies in a silver-coated fiber surrounded by air.

Figure 3 shows the modal index curves for a silver-coated fiber over an extended range of a to illustrate what happens to the TM_{0n} modes. These modes cut off at larger fiber diameters but if they are excited, then before they transfer energy to the SPP branch at the anticrossing points. Part of this energy will end up in the outer SPP at the fiber tip, as discussed further in Sec. III C.

III. MODE PROPAGATION TOWARDS THE TIP

A. Mode projection at the edge of the silver-coated region

Figure 1 shows that the silver layer is only present in the region $a \leq a_0$. At the edge of this region, the input field of the bare fiber taper is projected onto the eigenmode basis of the silver-coated fiber. If we initially assume that the input field is the TM_{01} mode of the bare fiber, the input energy is mostly transferred to the inner-SPP and TM_{01} modes of the silver-coated fiber. The mode projection efficiencies depend on the wavelength, the silver thickness, and the value of a_0 . Figure 4 shows the calculated mode projection efficiency P defined by [22]

$$P = \left| \frac{1}{2} \int_{A_\infty} [\hat{\mathbf{e}}_s(x, y) \times \hat{\mathbf{h}}_f(x, y)] \cdot \hat{\mathbf{a}}_z dA \right|^2, \quad (4)$$

where the subscripts f and s represent the mode in the bare fiber and the silver-coated fiber, respectively, the carets indi-

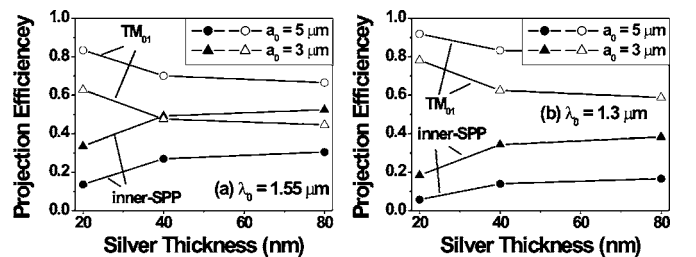


FIG. 4. Mode projection efficiencies from a TM_{01} mode of the bare fiber onto the inner-SPP (solid symbols) and TM_{01} (open symbols) modes of the silver-coated fiber. The wavelengths are (a) $1.55 \mu\text{m}$ and (b) $1.3 \mu\text{m}$. The edge of the silver coating is at $a_0 = 5 \mu\text{m}$ (circles) or $a_0 = 3 \mu\text{m}$ (triangles).

cate mode normalization, and the integration is over the infinite transverse cross section A_∞ .

Figure 4 shows that, as the silver thickness and wavelength increase, more energy is projected onto the inner SPP. Moving the edge of the silver coating towards the apex also increases the projection efficiency. In the remainder of this section we take the edge of the silver coating to be at $a_0 = 5 \mu\text{m}$, which is probably just practical from a fabrication point of view. For this value of a_0 , the mode projection efficiency onto the inner SPP is 30% for $\Delta = 80 \text{ nm}$ and $\lambda_0 = 1.55 \mu\text{m}$.

We now briefly consider the more realistic case that the input field is a superposition of the bare fiber eigenmodes. This is inevitable because the symmetry breaking associated with tapering of the fiber leads to coupling between all modes. The main effect is that more energy is projected onto the high-order modes of the silver-coated taper, which correspond to the lower mode branches in Fig. 3.

B. Intermodal coupling

All the modes excited at the silver coating edge couple with each other as they approach the apex because of the symmetry breaking mentioned above. The intermodal coupling can be treated analytically using coupled-mode theory [22]. We start by ignoring the imaginary part of the silver permittivity and take metal dissipation into account in the next section.

The transverse field distribution in each cross section of the fiber tip can be expanded in an orthonormal basis set of the local modes $\hat{\mathbf{e}}_j$ and $\hat{\mathbf{h}}_j$ as follows:

$$\mathbf{E}_t(x, y, z) = \sum_j b_j(z) \hat{\mathbf{e}}_{tj}[x, y, \beta_j(z)], \quad (5a)$$

$$\mathbf{H}_t(x, y, z) = \sum_j b_j(z) \hat{\mathbf{h}}_{tj}[x, y, \beta_j(z)], \quad (5b)$$

where the subscript t denotes the transverse component, $\beta_j(z)$ is the propagation constant, and $b_j(z)$ is the complex amplitude coefficient.

Before mode cutoff, the modal index difference between a forward guided mode and either radiation or backward modes is greater than that between two adjacent forward guided modes. The coupling from a forward guided mode to radiation or a backward mode is therefore weaker than that between forward modes and can be neglected. The coupled equations are given by [22]

$$db_j/dz = i\beta_j b_j + \sum_l C_{jl} b_l, \quad (6)$$

where the coupling coefficient between forward modes l and j is [22]

$$C_{jl} = \frac{\omega \epsilon_0}{4(\beta_j - \beta_l)} \int_{A_\infty} \hat{\mathbf{e}}_j^* \cdot \hat{\mathbf{e}}_l \frac{\partial n^2}{\partial z} dA. \quad (7)$$

The integral in Eq. (7) is ambiguous at a silver-dielectric interface because $\partial n^2 / \partial z$ behaves like a Dirac-delta function and the normal components of the electric fields are discon-

tinuous. However, in the Appendix, we show how this problem can be overcome by recasting Eq. (7) in the form

$$C_{jl} = \frac{\omega \epsilon_0}{4(\beta_j - \beta_l)} \int_{A_\infty} \left[\hat{\mathbf{e}}_{zj}^* \cdot \hat{\mathbf{e}}_{zl} + \frac{\hat{\mathbf{d}}_{rj}^* \cdot \hat{\mathbf{d}}_{rl}}{\epsilon^{(-)} \epsilon^{(+)}} \right] \frac{\partial n^2}{\partial z} dA, \quad (8)$$

where the subscripts z and r represent the longitudinal and radial components of the fields, \mathbf{d} is the electric displacement, and $\epsilon^{(-)} \epsilon^{(+)}$ is the product of the permittivity on either side of a silver-dielectric interface. Equation (8) is derived with the assumption that the metal permittivity is real.

C. Metal dissipation

Metal dissipation is approximately included in Eq. (6) by using a complex propagation constant in the first term and the coupling coefficient given by Eq. (8) in the second term. This is conceptually equivalent to subdividing each thin section of the silver-coated tapered fiber into an untapered absorbing section, in which there is dissipation but no mode coupling, and a tapered nonabsorbing section, in which there is mode coupling but no dissipation. This is a valid approximation because the effective indices of the local modes in these two kinds of sections are approximately equal in the near infrared.

Substituting the spatial distribution of dielectric constant $\epsilon(r, z) = \epsilon_{in} + (\epsilon_M - \epsilon_{in}) \vartheta(r - a(z)) + (\epsilon_{out} - \epsilon_M) \vartheta(r - b(z))$,

(9a)

$$\text{where } \vartheta(z) = \begin{cases} 0, & z < 0 \\ 1, & z > 0 \end{cases} \quad (9b)$$

into Eq. (8), we obtain the following expression for the coupling coefficient:

$$\begin{aligned} C_{jl}(z) = & \frac{\pi \omega \epsilon_0 \alpha}{2(\beta_j - \beta_l)} \{ [\hat{\mathbf{e}}_{zj}^*(r=a) \cdot \hat{\mathbf{e}}_{zl}(r=a) \\ & + (\epsilon_0^2 \epsilon_{in} \epsilon_M)^{-1} \hat{\mathbf{d}}_{zj}^*(r=a) \cdot \hat{\mathbf{d}}_{zl}(r=a)] (\epsilon_M - \epsilon_{in}) a(z) \\ & + [\hat{\mathbf{e}}_{zj}^*(r=b) \cdot \hat{\mathbf{e}}_{zl}(r=b) + (\epsilon_0^2 \epsilon_{out} \epsilon_M)^{-1} \hat{\mathbf{d}}_{zj}^*(r=b) \\ & \cdot \hat{\mathbf{d}}_{zl}(r=b)] (\epsilon_{out} - \epsilon_M) b(z) \}. \end{aligned} \quad (10)$$

The coupling coefficient is proportional to the taper angle α while the length of the fiber tip is inversely proportional to α . The effective coupling between two guided modes is therefore nearly independent of α . In the following calculations we investigate intermodal coupling for a taper angle of 5° .

Initially, we assume that only the inner SPP of the silver-coated fiber is excited at the edge of the coating located at a radius $a_0 = 5 \mu\text{m}$ and restrict coupling to adjacent modes. Figure 5 shows the modal energy evolution of the SPP branch in Fig. 3 with fiber radius a for a range of wavelengths and silver thickness. The effect of metal dissipation manifests itself in the finite slope. As the silver thickness decreases, metal dissipation and thus propagation loss increase because there is a greater fraction of the SPP field in the metal [26]. For large silver thickness intermodal coupling

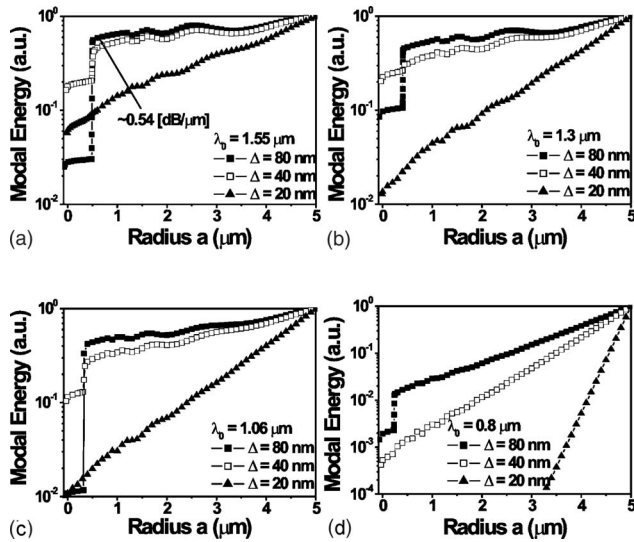


FIG. 5. Mode energy (in arbitrary units) of the SPP branch in Fig. 3 as a function of the fiber radius a for different wavelengths (λ_0) and silver thickness (Δ). The taper angle is 5° .

leads to an undulation in the evolution curves and a step down at the anticrossing point. Note that only 2 or 3% of the energy in the inner SPP is transferred into the outer SPP for an 80-nm-thick silver film at a wavelength of $1.06 \mu\text{m}$. For similar conditions, the authors of Ref. [14] report a figure of 46% in a perturbation theory treatment that neglects the hybridized nature of the SPP modes. As the silver thickness decreases, the anticrossing gap between branches widens, as shown in Figs. 2(a) and 2(e). The mode-coupling coefficient therefore decreases due to the increase of $\beta_j - \beta_l$ in Eq. (10) and the downward step is reduced. The silver thickness is an important parameter in the design optimization since it determines the tradeoff between metal dissipation and intermodal coupling strength.

Another important design parameter is the wavelength. When the wavelength decreases, the absolute value of the real part of the silver dielectric constant decreases and the imaginary part increases. This has the consequence that the outer and inner SPPs penetrate more deeply into the metal and interact more strongly. This widens the anticrossing gap, as shown in Figs. 2(a) and 2(f), reduces the intermodal coupling coefficient, and increases dissipation, as shown in Fig. 5.

We now consider the case where the input field is the TM_{01} mode of the bare fiber. The edge of the coating is taken to be at $a_0 = 5 \mu\text{m}$, the silver thickness is 80 nm, the wavelength is $1.55 \mu\text{m}$, and the other parameters are the same as those in Fig. 5(a). The energy evolution of the SPP and TM_{01} mode branches in the silver-coated fiber is shown in Fig. 6 which displays the effects of mode projection, metal dissipation, and intermodal coupling. In contrast to the downward steps shown in Fig. 5, intermodal coupling here results in an upward step in the modal energy of the SPP branch at the anticrossing point. Nearly all the energy in the TM_{01} mode is transferred to the inner SPP. The solid line in Fig. 6 is the combined energy of the SPP and TM_{01} branches. The slope ($\sim 0.29 \text{ dB per micron}$ decrease in radius) is less than that in

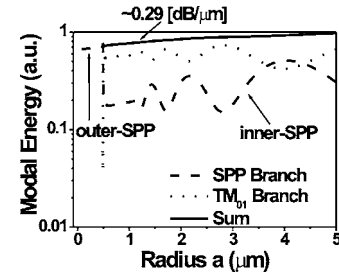


FIG. 6. Mode energy of the SPP branch (dashes) and the TM_{01} branch (dots) as a function of the radius a . The taper angle, silver thickness, and wavelength are 5° , 80 nm, and $1.55 \mu\text{m}$, respectively. The solid curve is the sum of the dashed and dotted curves.

Fig. 5(a) ($\sim 0.54 \text{ dB}/\mu\text{m}$) because the TM_{01} mode has less field overlap with the metal coating than the inner SPP and there is less dissipation.

As mentioned above, the input field will in practice be more complicated than assumed in Figs. 5 and 6 because of mode coupling in the bare tapered fiber region. The input energy is projected onto the set of radially polarized eigenmodes of the silver-coated fiber. The high-order modes suffer less metal dissipation with their smaller field-silver overlap. At anticrossing points, intermodal coupling is enhanced because of the closer approach of the mode branches. The example in Fig. 6 shows that a significant fraction of the energy in higher-order modes can be transferred to the outer SPP at the apex. If the energy is instead coupled into the lower mode branches, it is transported away from the fiber tip by radiation and reflection. The influence of input mode projection on the energy conversion efficiency is a complicated, structure specific problem that lies outside the range of our more general investigation.

IV. RADIATION COUPLING IN THE VICINITY OF THE APEX

When the fiber radius decreases below that for mode cutoff, only the outer SPP remains so that it can only couple with radiation. Radiation coupling depends on the taper angle and influences both transverse field confinement and propagation loss. It is difficult to deal with analytically because radiation only takes energy away from the waveguide so that the interaction length between radiation and guided modes is ill defined. In the following two sections, we first consider a qualitative treatment of radiation loss based on the criterion for adiabatic propagation, and then describe a more quantitative study based on the finite integration technique.

A. Adiabaticity criterion

For adiabatic propagation, the local taper length scale needs to be larger than the coupling length of relevant modes [27]. The local taper length scale L_t is the height of the circular cone whose base is coincident with the local cross section, and whose apex angle is equal to the local taper angle. The coupling length of two modes, L_b , is taken to be the beat length. The two lengths can be expressed as [27]

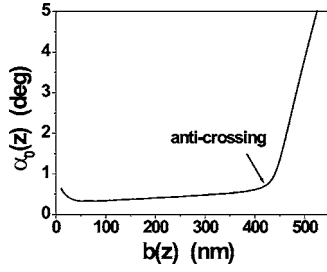


FIG. 7. Critical taper angle for adiabatic propagation as a function of outer radius b . The silver thickness is 40 nm and the wavelength is 1.3 μm .

$$L_t(z) \approx b(z)/\alpha, \tag{11a}$$

$$L_b(z) \approx 2\pi/\text{Re}[\beta_1(z) - \beta_2(z)], \tag{11b}$$

where β_1 and β_2 are the propagation constants of the outer SPP and radiation, respectively, and Eq. (11b) is a crude approximation.

The silver-coated fiber tip is surrounded by air, therefore we assume that the effective modal index of the radiation is unity. The adiabaticity criterion $L_t > L_b$ thus leads to the requirement

$$\alpha(z) < \alpha_0(z) = b(z)\text{Re}[n_1(z) - 1]/\lambda_0, \tag{12}$$

where $\alpha_0(z)$ is the critical taper angle for adiabatic propagation and $n_1(z)$ is the effective mode index of the outer SPP.

Figure 7 shows the variation of $\alpha_0(z)$ with the outer fiber radius b . It is clear that the adiabaticity requirement is easily satisfied above the anticrossing point but is difficult to satisfy below. Therefore, radiation coupling mainly occurs in the vicinity of the silver apex, where the outer SPP is excited and the field lies largely outside the fiber. This result is consistent with the behavior of the modal coupling coefficient described by Eq. (10) in which C increases as $b^{-1/2}$ as the tip is approached. This is because the propagation constant varies with radius as $\beta \sim b^{-1}$ and the electric field as $|E_{z,r}| \sim b^{-3/2}$ [16].

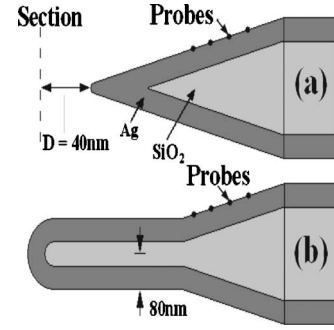


FIG. 8. Schematic of (a) structure 1 and (b) structure 2 used in numerical simulations.

B. Numerical simulations

Using the finite integration technique [28], numerical simulations were carried out on the structure shown in Fig. 8(a), which we call structure 1. The silver thickness is 40 nm and the inner fiber radius a is 140 nm at the wider end which is below the anticrossing radius. A broadband radially polarized pulse was injected from the right-hand side and the fields at successive time steps were calculated using a commercial FIT package [29]. Before entering the fiber tip region, the input wave propagates through a 4- μm -long uniform cylindrical waveguide which helps to establish the true field profile of the outer SPP. The frequency-dependent silver dielectric function was approximated by a Drude model, which is in very good agreement with the Drude-Lorentz model used in the previous analytical calculations. The simulated fiber tip only supports a single guided mode (the outer SPP), so that the results reflect the effects of radiation coupling and metal dissipation.

Figure 9 shows the calculated distribution of the electric field amplitude. As expected, the results demonstrate that the field is strongly enhanced at the apex. The longitudinal fringes arise from interference between incident and reflected pulses. Figures 10(a) and 10(c) show the radial distribution of the longitudinal and radial components of the electric field 40 nm behind the silver apex [at the plane section shown in

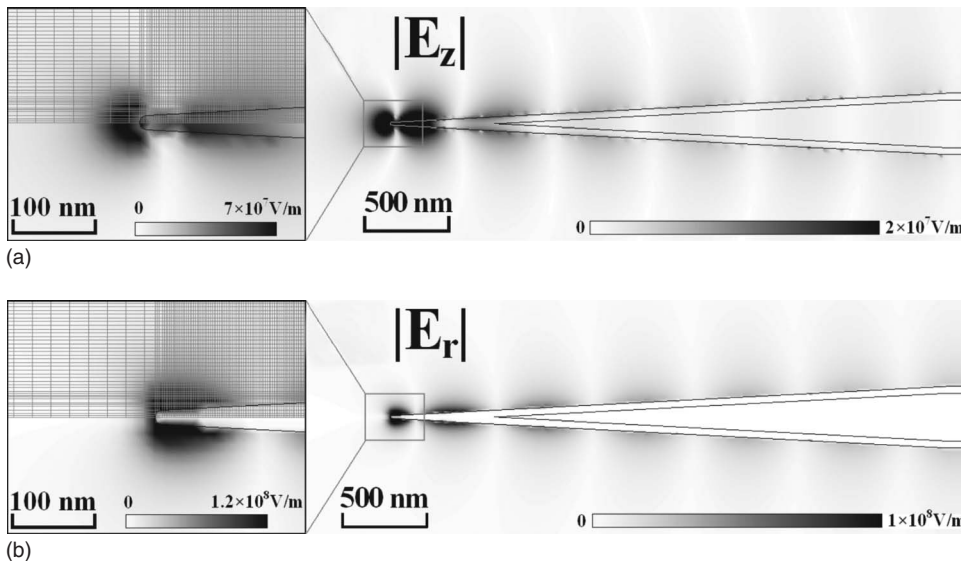


FIG. 9. Calculated distributions of (a) $|E_z|$ and (b) $|E_r|$ for $\lambda_0 = 1.3 \mu\text{m}$. Dark areas correspond to a stronger field. The lattices in the magnified windows are the simulation meshes. The taper angle is 3° and the silver thickness is 40 nm.

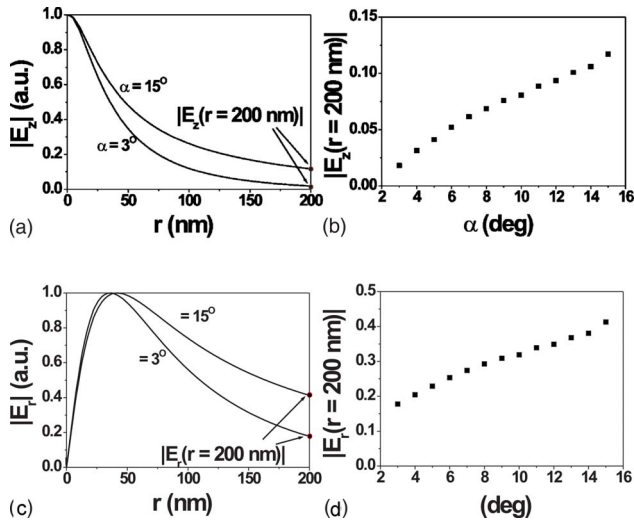


FIG. 10. (Color online) Radial variation of (a) $|E_z|$ and (c) $|E_r|$ over the cross section shown in Fig. 9(a). The section is in air and 40 nm from the silver apex. (b) and (d) show the field amplitudes at $r=200$ nm as a function of taper angle.

Fig. 8(a)]. As the taper angle increases from 3° to 15° , radiation coupling increases and causes a reduction in the transverse field confinement as shown in Figs. 10(b) and 10(d).

In addition to transverse field confinement, radiation coupling influences the propagation loss. In order to quantify this effect, we recorded the time variations of the magnetic field at a series of probe points arranged along the outer silver surface, as indicated in Fig. 8(a). The contribution to the probe signals from the wave reflected from the apex was subtracted and the frequency-domain amplitudes at $\lambda = 1.3 \mu\text{m}$ were then used to calculate the mode energy of the outer SPP integrated over the cross section at each position. We assume that all guided energy is confined in the local mode of the outer SPP, for which the field distribution is known for a given magnetic field amplitude at the outer silver surface. Because the outer SPP field is enhanced at the surface whereas the radiation field varies slowly with radius, the two fields can be separated. The solid symbols in Fig. 11(a) show the outer-SPP mode energy variation with radius b for a taper angle of 3° . For comparison, the mode energy calculated using Eq. (6) is shown by the solid curve. This calculation ignores radiation coupling but takes into account metal dissipation. The close agreement of the two results reflects the minimal influence of radiation coupling at this small taper angle.

For a larger taper angle, the length of the silver-coating region is smaller and the reflected pulse from the apex overlaps the forward pulse in time and is hard to subtract. In order to overcome this difficulty, we used a second simulation structure shown in Fig. 8(b). Here, an additional $1.5\text{-}\mu\text{m}$ -long uniform waveguide is attached to the fiber tip to increase the delay of the reflected pulse. Although the discontinuity associated with this structure also introduces a reflection, this was minimized by adjusting the attachment position to be at $b=80$ nm. The symbols in Fig. 11(b) show

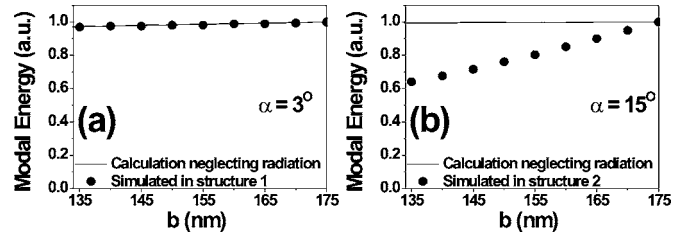


FIG. 11. Mode energy evolution as a function of the outer radius of the silver coating, b , for a fiber tip with taper angles of (a) 3° and (b) 15° . The symbols show results obtained from numerical simulations which include the effect of radiation coupling. The solid curves show calculations which include metal dissipation but ignore radiation. The silver thickness and the wavelength are 40 nm and $1.3 \mu\text{m}$, respectively.

the modal energy evolution for $\alpha=15^\circ$. The large deviation from the analytical calculation (solid curve) is due to strong radiation coupling.

In Fig. 11, the difference between the simulated and calculated curves is a measure of the radiative loss in the region from $b=135$ nm to $b=175$ nm. Figure 12 shows the increase of this propagation loss with taper angle. The data is made up from the results of simulations using both fiber tip structures. The dip in the data from structure 2 at larger angles is probably due to a residual effect of the reflection from the apex mentioned above. For small taper angles the simulated results from structures 1 and 2 are consistent. The solid curve is a guide to the eye and indicates the probable enhancement of the radiation coupling loss with increasing taper angle.

V. DISCUSSION

To maximize the conversion efficiency from fiber waveguide modes to the outer SPP at the silver apex, the wavelength, taper angle, and length and thickness of the silver coating need to be optimized. This optimization involves trade-offs between the effects of mode projection, intermodal coupling, metal dissipation, and radiation coupling.

Mode projection is influenced by the wavelength, silver thickness, and fiber radius at the edge of the silver-coated

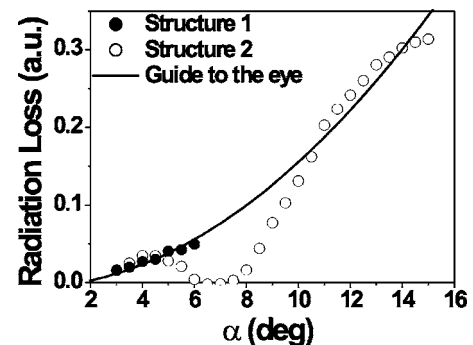


FIG. 12. Radiative propagation loss as a function of the taper angle α . The solid symbols are results obtained for structure 1 [Fig. 9(a)], and the open symbols for structure 2 [Fig. 9(b)]. The silver thickness and the wavelength are 40 nm and $1.3 \mu\text{m}$, respectively. The solid curve is a guide to the eye.

TABLE I. Relationships between the mode conversion mechanisms and the structural parameters of a silver-coated fiber tip.

Parameter \ Mechanism	Taper angle	Wavelength	Silver thickness	Fiber radius at edge of silver coating
	Mode projection (to the lower mode)		+	+
Intermodal coupling		+	+	
Metal dissipation	-	-	-	
Radiation coupling	+			

region (i.e., proximity to the apex for a given taper angle). A long wavelength, a thick silver coating, and close proximity of the silver coating edge to the apex allow more energy to be projected onto the SPP branch. However, energy projected onto high-order modes (TM_{0n} modes) also couples to the outer SPP via mode anticrossings. The TM_{0n} modes suffer less metal dissipation during propagation toward the silver apex and coupling to the outer SPP can be efficient.

The strength of intermodal coupling is principally affected by the silver thickness and wavelength. Decreasing either one increases the mode interaction and results in a larger gap between adjacent mode branches, which reduces intermodal coupling. The effect of intermodal coupling on mode conversion is complicated and depends on the input field, the coupling strength, and the length of the metal-coated region.

Metal dissipation is mainly influenced by the wavelength, silver thickness, and taper angle. A short wavelength causes enhanced field penetration into the silver layer and an increase of the imaginary part of the metal's dielectric constant. A thin silver layer leads to a large overlap with the SPP field due to the mode symmetry [26]. A small taper angle increases the fiber tip length. All these factors increase metal dissipation and lower the efficiency of mode conversion.

The only important parameter affecting radiation coupling is the taper angle. As the angle increases, both the transverse field confinement at the silver apex and the radiation-induced propagation loss become worse.

Table I summarizes the above effects and how they are influenced by the structural parameters. A blank entry indicates a negligible influence of the parameter on an effect. The symbols + and - indicate an increase or decrease in the size of the effect with an increase in the value of the parameter.

It is useful to try and place a lower limit on the efficiency of power transfer from radially polarized waveguide modes of the bare tapered fiber to the outer SPP. Let us consider a wavelength and silver thickness close to $1.55 \mu\text{m}$ and 80 nm , respectively. If we choose a taper angle of 5° and a coating length of $57 \mu\text{m}$ corresponding to a value for a_0 of $5 \mu\text{m}$ then, according to Fig. 4, the projection efficiency onto the inner SPP from a TM_{01} bare fiber mode is approximately 30% while that onto the TM_{01} mode is around 70%. Approximately 60% of the total energy is then transferred to the outer SPP at the apex (Fig. 6) due to the negligible radiation loss (Fig. 11). In practice, energy will be shared with higher-

order modes so that the net energy transfer efficiency could be higher or lower. We have not considered the effect of surface roughness or other imperfections which are likely to lower the efficiency. On the other hand, the parameters of the structure just discussed are not optimized. On balance, it seems unlikely that in an optimized structure the conversion efficiency would be less than 10%.

VI. CONCLUSIONS

In this paper, we have theoretically investigated the process in which optical fiber waveguide modes are converted into a plasmon polariton on the outer surface of a silver-coated fiber tip. The conversion fundamentally results from mode anticrossings. Our investigation highlights the mechanisms and relative importance of mode projection, mode coupling, metal dissipation, and radiation loss which must be taken into account in order to achieve efficient energy transfer to the tip. The conversion efficiency depends on the details of the structure but is expected to be at least 10%. This improvement in efficiency by several orders of magnitude compared with external excitation is very promising for applications in high dynamic range near-field optical microscopy and spectroscopy. Our calculations have been performed ignoring nonlinear optical effects in the fiber waveguide but they could, in principle, be extended to take these into account. We anticipate that delivery of intense optical pulses to the fiber tip might allow the study of optical nonlinearities on the nanoscale.

ACKNOWLEDGMENT

This work was supported by the Engineering and Physical Sciences Research Council (EPSRC).

APPENDIX

Here, we present the derivation of Eq. (8) from Eq. (7). We start by introducing the positive-limiting differential definition as follows:

$$\frac{\partial^{(+)}f(z)}{\partial z} = \lim_{\Delta z \rightarrow 0^+} \frac{f(z + \Delta z) - f(z)}{\Delta z}, \quad (\text{A1})$$

where the function $f(z)$ can be discontinuous but has to be finite. Using this definition, we obtain

$$\frac{\partial^{(+)}[n^2(z)\hat{\mathbf{e}}(z)]}{\partial z} = n^2(z)\frac{\partial^{(+)}\hat{\mathbf{e}}(z)}{\partial z} + \frac{\partial^{(+)}n^2(z)}{\partial z}\hat{\mathbf{e}}(z+),$$

$$\begin{aligned} \frac{\partial^{(+)}[\beta(z)\hat{\mathbf{a}}_z \times \hat{\mathbf{e}}(z)]}{\partial z} &= \beta(z)\hat{\mathbf{a}}_z \times \frac{\partial^{(+)}\hat{\mathbf{e}}(z)}{\partial z} \\ &+ \frac{\partial^{(+)}\beta(z)}{\partial z}[\hat{\mathbf{a}}_z \times \hat{\mathbf{e}}(z+)], \end{aligned}$$

$$\frac{\partial^{(+)}[\beta(z)\hat{\mathbf{a}}_z \times \hat{\mathbf{h}}(z)]}{\partial z} = \beta(z)\hat{\mathbf{a}}_z \times \frac{\partial^{(+)}\hat{\mathbf{h}}(z)}{\partial z} + \frac{\partial^{(+)}\beta(z)}{\partial z}[\hat{\mathbf{a}}_z \times \hat{\mathbf{h}}(z)], \quad (\text{A2a})$$

where

$$\hat{\mathbf{e}}(z+) = \lim_{\Delta z \rightarrow 0^+} \hat{\mathbf{e}}(z + \Delta z), \quad \hat{\mathbf{h}}(z+) = \lim_{\Delta z \rightarrow 0^+} \hat{\mathbf{h}}(z + \Delta z). \quad (\text{A2b})$$

Applying Maxwell's equations to the j th and l th local modes of a cylindrical waveguide, we obtain

$$i\omega\mu_0\hat{\mathbf{h}}_j(z) = \nabla_t \times \hat{\mathbf{e}}_j(z) + i\beta_j(z)\hat{\mathbf{a}}_z \times \hat{\mathbf{e}}_j(z), \quad (\text{A3a})$$

$$-i\omega\varepsilon_0 n^2(\mathbf{r})\hat{\mathbf{e}}_j(z) = \nabla_t \times \hat{\mathbf{h}}_j(z) + i\beta_j(z)\hat{\mathbf{a}}_z \times \hat{\mathbf{h}}_j(z), \quad (\text{A3b})$$

$$i\omega\mu_0\hat{\mathbf{h}}_l(z) = \nabla_t \times \hat{\mathbf{e}}_l(z) + i\beta_l(z)\hat{\mathbf{a}}_z \times \hat{\mathbf{e}}_l(z), \quad (\text{A3c})$$

$$-i\omega\varepsilon_0 n^2(\mathbf{r})\hat{\mathbf{e}}_l(z) = \nabla_t \times \hat{\mathbf{h}}_l(z) + i\beta_l(z)\hat{\mathbf{a}}_z \times \hat{\mathbf{h}}_l(z), \quad (\text{A3d})$$

where the subscripts t and z represent the transverse and longitudinal components. The only important assumption that we have made so far is that the dielectric constant $n^2(\mathbf{r})$ is real, i.e., the waveguide is nonabsorbing.

Performing the operation

$$(A3a)^* \cdot \frac{\partial^{(+)}\hat{\mathbf{h}}_l}{\partial z} + (A3b)^* \cdot \frac{\partial^{(+)}\hat{\mathbf{e}}_l}{\partial z} + \frac{\partial^{(+)}(A3c)}{\partial z} \cdot \hat{\mathbf{h}}_j^* + \frac{\partial^{(+)}(A3d)}{\partial z} \cdot \hat{\mathbf{e}}_j^*$$

on Eqs. (A3a)–(A3d) we obtain

$$\begin{aligned} & \omega\varepsilon_0 n^2(\mathbf{r})' \cdot \hat{\mathbf{e}}_j^* \cdot \hat{\mathbf{e}}_l(z+) \\ &= -i\nabla_t \cdot (\hat{\mathbf{e}}_j^* \times \hat{\mathbf{h}}_l' + \hat{\mathbf{e}}_l' \times \hat{\mathbf{h}}_j^*) + \beta_l' \hat{\mathbf{a}}_z \cdot [\hat{\mathbf{e}}_l(z+) \times \hat{\mathbf{h}}_j^*(z+) \\ & \quad - \hat{\mathbf{h}}_l \times \hat{\mathbf{e}}_j^*] + (\beta_l - \beta_j)\hat{\mathbf{a}}_z \cdot [\hat{\mathbf{e}}_j^* \times \hat{\mathbf{h}}_l' - \hat{\mathbf{h}}_j^* \times \hat{\mathbf{e}}_l'], \end{aligned} \quad (\text{A4})$$

where the asterisks represent complex conjugation and the positive-limiting differential definition in Eq. (A1) and the magnetic field boundary continuity condition $\hat{\mathbf{h}}(z+) = \hat{\mathbf{h}}(z)$ are used.

Integrating Eq. (A4) over an infinite cross sectional area (A_∞) and applying the two-dimensional form of the divergence theorem, we obtain

$$\begin{aligned} C_{jl}^{(+)}(z) &= \frac{1}{4} \int_{A_\infty} \left[\hat{\mathbf{h}}_j^* \times \frac{\partial^{(+)}\hat{\mathbf{e}}_l}{\partial z} - \hat{\mathbf{e}}_j^* \times \frac{\partial^{(+)}\hat{\mathbf{h}}_l}{\partial z} \right] \cdot \mathbf{a}_z dA \\ &= \frac{\omega\varepsilon_0}{4(\beta_j - \beta_l)} \int_{A_\infty} \hat{\mathbf{e}}_j^* \cdot \hat{\mathbf{e}}_l(z+) \frac{\partial^{(+)}n^2}{\partial z} dA. \end{aligned} \quad (\text{A5})$$

Similarly, a coupling coefficient $C_{jl}^{(-)}$ can be derived from a negative-limiting differential definition analogous to Eq. (A1). The result is

$$\begin{aligned} C_{jl}^{(-)}(z) &= \frac{1}{4} \int_{A_\infty} \left[\hat{\mathbf{h}}_j^* \times \frac{\partial^{(-)}\hat{\mathbf{e}}_l}{\partial z} - \hat{\mathbf{e}}_j^* \times \frac{\partial^{(-)}\hat{\mathbf{h}}_l}{\partial z} \right] \cdot \mathbf{a}_z dA \\ &= \frac{\omega\varepsilon_0}{4(\beta_j - \beta_l)} \int_{A_\infty} \hat{\mathbf{e}}_j^* \cdot \hat{\mathbf{e}}_l(z-) \frac{\partial^{(-)}n^2}{\partial z} dA. \end{aligned} \quad (\text{A6})$$

When applied to a metal-coated fiber tip, the results of Eqs. (A5) and (A6) are identical. The coupling coefficient in Eq. (7) can therefore be expressed as

$$\begin{aligned} C_{jl}(z) &= \frac{1}{4} \int_{A_\infty} \left[\hat{\mathbf{h}}_j^* \times \frac{\partial \hat{\mathbf{e}}_l}{\partial z} - \hat{\mathbf{e}}_j^* \times \frac{\partial \hat{\mathbf{h}}_l}{\partial z} \right] \cdot \hat{\mathbf{a}}_z dA = C_{jl}^{(+)}(z) \\ &= C_{jl}^{(-)}(z) = \frac{\omega\varepsilon_0}{4(\beta_j - \beta_l)} \int_{A_\infty} \left[\hat{\mathbf{e}}_{zj}^* \cdot \hat{\mathbf{e}}_{zl} + \frac{\hat{\mathbf{d}}_{rj}^* \cdot \hat{\mathbf{d}}_{rl}}{\varepsilon^{(-)}\varepsilon^{(+)}} \right] \frac{\partial n^2}{\partial z} dA, \end{aligned} \quad (\text{A7})$$

where the subscripts z and r represent the longitudinal and radial components of the fields, respectively, \mathbf{d} is the electric displacement, and $\varepsilon^{(-)}\varepsilon^{(+)}$ is the product of the permittivities on either side of a metal-dielectric interface. Unlike Eq. (7), the second integral in Eq. (A7), which is the same as Eq. (8), is unambiguous.

-
- [1] M. Ohtsu and H. Hori, *Near-Field and Nano-Optics* (Kluwer Academic, New York, 1999).
 [2] D. W. Pohl, W. Denk, and M. Lanz, *Appl. Phys. Lett.* **44**, 651 (1984).
 [3] A. Lewis, M. Isaacson, A. Harootunian, and A. Muray, *Ultramicroscopy* **13**, 227 (1984).
 [4] E. Betzig, J. K. Trautman, T. D. Harris, J. S. Weiner, and R. L. Kostelak, *Science* **251**, 1468 (1991).
 [5] E. Betzig and J. K. Trautman, *Science* **257**, 189 (1992).
 [6] M. Ashino and M. Ohtsu, *Appl. Phys. Lett.* **72**, 1299 (1998).
 [7] P. M. Adam, P. Royer, R. Laddada, and J. L. Bijeon, *Appl. Opt.*

- 37**, 1814 (1998).
 [8] E. J. Sanchez, L. Novotny, and X. S. Xie, *Phys. Rev. Lett.* **82**, 4014 (1999).
 [9] R. Eckert, J. M. Freyland, H. Gersen, and H. Heinzelmann, *Appl. Phys. Lett.* **77**, 3695 (2000).
 [10] F. Zenhausern, M. P. O'Boyle, and H. K. Wickramasinghe, *Appl. Phys. Lett.* **65**, 1623 (1994).
 [11] A. Bouhelier, J. Renger, M. R. Beversluis, and L. Novotny, *J. Microsc.* **210**, 220 (2003).
 [12] M. I. Stockman, *Phys. Rev. Lett.* **93**, 137404 (2004).
 [13] L. Vaccaro, L. Aeschmann, U. Staufner, H. P. Herzig, and R.

- Dandliker, Appl. Phys. Lett. **83**, 584 (2003).
- [14] N. A. Janunts, K. S. Baghdasaryan, Kh. V. Nerkararyan, and B. Hecht, Opt. Commun. **253**, 118 (2005).
- [15] L. Novotny and C. Hafner, Phys. Rev. E **50**, 4094 (1994).
- [16] A. J. Babadjanyan, N. L. Margaryan, and Kh. V. Nerkararyan, J. Appl. Phys. **87**, 3785 (2000).
- [17] R. G. Milner and D. Richards, J. Microsc. **202**, 66 (2001).
- [18] B. Prade, J. Y. Vinet, and A. Mysyrowicz, Phys. Rev. B **44**, 13556 (1991).
- [19] C. Rhode, K. Hasegawa, and M. Deutsch, Opt. Lett. **32**, 415 (2007).
- [20] A. D. Rakic, A. B. Djurisic, J. M. Elazar, and M. L. Majewski, Appl. Opt. **37**, 5271 (1998).
- [21] R. Ruppin, Phys. Lett. A **340**, 299 (2005).
- [22] A. W. Snyder and J. D. Love, *Optical Waveguide Theory* (Chapman and Hall, London, 1983).
- [23] T. Grosjean, A. Sabac, and D. Courjon, Opt. Commun. **252**, 12 (2005).
- [24] S. Quabis, R. Dorn, and G. Leuchs, Appl. Phys. B: Lasers Opt. **81**, 597 (2005).
- [25] A. Ishimaru, *Electromagnetic Wave Propagation, Radiation, and Scattering* (Prentice-Hall, Englewood Cliffs, 1991).
- [26] S. J. Al-Bader and M. Imtaar, IEEE J. Quantum Electron. **28**, 525 (1992).
- [27] J. D. Love, W. M. Henry, W. J. Stewart, R. J. Black, S. Lacroix, and F. Gonthier, IEE Proc.-J: Optoelectron. **138**, 343 (1991).
- [28] T. Weiland, Int. J. Electron. **31**, 116 (1977).
- [29] CST MICROWAVE STUDIO 2006.